European Journal of Control (2004)10:174–186

European Journal of Control

System Identification and Multivariable Control Design for a Satellite UltraQuiet Isolation Technology Experiment (SUITE)

Alok Joshi and Won-jong Kim

Texas A&M University, College Station, TX 77843-3123, USA

The main objective of the 'Satellite UltraQuiet Isolation Technology Experiment' is to attenuate the vibration in the braodband up to 100 Hz, and at 5-, 25-, and 100-Hz corner frequencies in a six-degree-of-freedom hexapod system mounted on a satellite. To design the controller for vibration isolation, the identification of the plant transfer function was necessary. The hexapod assembly model was identified using various band-limited test signals such as chirp, white Gaussian noise, and pseudo-random binary signals. Using the observed responses to these test signals, a 6×6 transfer function matrix relating six piezo-actuator input voltages and the six geophone-sensor output voltages was obtained in the discrete-time domain. Various model structures such as auto-regression with exogeneous inputs, auto-regression moving-average with exogeneous inputs, and Box–Jenkins (BJ) were used for system identification. The transfer functions obtained by a fifth-order BJ model were validated in the time and frequency domains. Their orders were matched with the order of the electro-mechanical model of the combined piezo-geophone system. Various multi-input multi-output control design methodologies such as linear quadratic Gaussian and H^{∞} were proposed for active vibration isolation up to 100 Hz. The simulation results using these controllers achieved 33- and 12-dB attenuation at 5- and 25-Hz corner frequencies, respectively.

Keywords: Active Vibration Isolation; Control Methodology; Hexapod; System Identification; Validation

Nomenclature

V_{aj}	Voltage applied to the jth piezoelectric actuator (V)
V_{gi}	Voltage measured from the ith geophone sensor (V)
V_{in}	Input voltage for the piezoelectric actuator model (V)
V_{out}	Output voltage for the geophone sensor model (V)
V_{RC}	Voltage drop across the Maxwell circuit (V)
F_{ext}	External mechanical load on the actuator (N)
q	Total charge in the circuit for the actuator electrical model (C)
n	Electromechanical transformer ratio (C/m)
x	Displacement of the mass m_p of the actuator and geophone base (m)
y	Absolute displacement of the coil of the geophone sensor (m)
N	Number of turns of the geophone coil
C	Linear capacitance in parallel with the transformer (F)

Correspondence to: Won-jong Kim, Texas A&M University, College Station, TX 77843-3123, USA. E-mail: wjkim@mengr.tamu.edu

Received 24 March 2003; Accepted 15 November 2003. Recommended by E. Mosca and D. Clarke.

F_t	Transduced force from the electrical domain of the actuator model (N)
V_t	Back emf from the mechanical domain of the actuator model (V)
ϕ_g	Flux linkage per turn of the geophone coil (Wb)
X	Absolute motion of the geophone base/body (m)
Y	Absolute motion of moving coil of the geophone sensor (m)
$z = y - x$	Displacement of the coil relative to the permanent magnet (m)
C_M, R_M	Capacitance and resistance in the Maxwell circuit (F, Ω)
m_p, b_p, k_p	Equivalent mass, damping coefficient and stiffness for the piezoelectric actuator model, respectively (kg, N-s/m, N/m)
m_g, b_g, k_g	Equivalent mass, damping coefficient and stiffness for the geophone sensor model, respectively (kg, N-s/m, N/m)

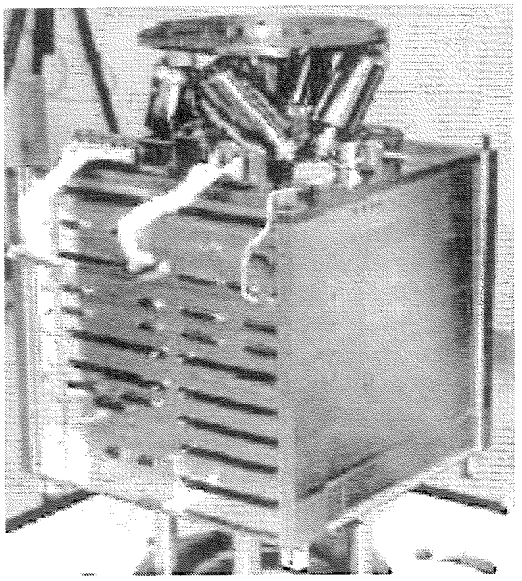

Fig. 1. The PICOsatellite is a micro-satellite acquired by the Air Force Test Program and manufactured by Surrey Satellite Technology Limited (SSTL) of Guildford, Surrey, England. Courtesy of United States Air Force Research Laboratory, Kirtland Air Force Base, New Mexico [1].

1. Introduction

A hexapod consists of a movable platform connected to the fixed base by six variable-length struts. The length of each strut can be controlled independently by six linear actuators and sensors to achieve independent translational and rotational motions along the x-, y-, and z-axes giving six degrees of freedom (6 DOFS) to the platform. The hexapod has higher stiffness and payload-to-weight ratio compared to other 6-DOF systems. Passive dampers located in each strut work in combination with variable-length actuators in such a way that the heat dissipation from the damper and the change in the length of the actuators compensate the vibration transmitted from the base to the platform. This combined active-passive hexapod vibration isolator is widely accepted in the applications such as next-generation machine tools [7,17], space structure positioning and pointing systems [16], and active optics [11].

'Satellite UltraQuiet Isolation Technology Experiment (SUITE)' [1] is intended to provide a quiet platform for precision sensors on the noisy PICOsatellite shown in Fig. 1. We conducted various experiments to model the 6-DOF hexapod mounted on the PICOsatellite and developed algorithms for vibration isolation through the SUITE Guest Investigator Program at Air Force Research Laboratory (AFRL). The main objective of this experiment is to attenuate the vibration in the frequency range of 5 100 Hz. Initially, the algorithms were tested on identical ground-unit and then on the orbiting satellite. For the ground-unit, vibrations due to motors or torque coils are transmitted to ground besides various components on the ground-unit considered for vibration attenuation. However, orbiting satellite behaves like a lightly damped system where vibration attenuation at high corner frequencies is hard to achieve.

In this paper, system identification approaches such as auto regression with exogeneous variables (ARX), auto regression moving average with exogeneous variables (ARMAX), and Box–Jenkins (BJ) model structures were selected for the estimation of the transfer function matrix relating the six piezo-actuator inputs to the six geophone sensor outputs for the hexapod system. A 6-DOF hexapod system can be mathematically modeled in several ways. Various methods such as the Newton–Raphson method with first-order gradient correction for calculation of the Jacobian and inverse-Jacobian, the One Point Iteration method or a Homotopy method can be used for closed-form kinematics solutions for hexapod systems [9,10,18]. Modeling of a hexapod on the basis of stiffness and stability is another approach [13,15,19]. These methods define the relationship between position of the platform and six strut lengths. The majority of these methods assume that hexapod is in cubic configuration, i.e., hexapod struts are orthogonal.

This assumption neglects coupling among the struts for simplifying calculations. However, hexapod used in SUITE is not in cubic configuration. In this paper we find the relation between the six piezoelectric actuator input voltages and the six geophone sensor output voltages. This approach enabled us to study effect of cross coupling and capture it in our empirically-derived mathematical model in terms of transfer functions. A 6×6 transfer function matrix identified using various system identification techniques can be used for control. Various vibration attenuation methods such as direct adaptive disturbance rejection, robust adaptive filtering, and decoupled controller design have been used [3–5]. These approaches used six channels of single-input single-output (SISO) controllers assuming that there is no coupling among the variables. Considering the effect of cross-coupling, we designed multivariable controllers for improvement in active isolation of the hexapod platform from the incoming base-vibrations. The simulation results using these controllers achieved 33- and 12-dB attenuation at 5- and 25-Hz corner frequencies, respectively.

This paper describes the 6-DOF SUITE hexapod assembly, hardware, and software used for data acquisition, actuation, and control. The main emphasis will be given on the selection of the structures for mathematical modeling of the SUITE hexapod and model validation. System identification using a chirp signal and band-limited white Gaussian noise is performed experimentally to find the transfer-function matrix in the discrete-time domain. The paper concludes with the demonstration of vibration attenuation obtained during the simulation of linear quadratic Gaussian/loop transfer function recovery (LQG/LTR) and H^{∞} multivariable controller. These results with time- and frequency-domain validation, support the accuracy of mathematical model.

2. Description of the SUITE Hexapod System

2.1. Hardware

As shown in Fig. 2, the SUITE hexapod hardware consists of a movable platform connected to the fixed base by six identical struts with various actuators, sensors, and a tray module containing a microcontroller and a digital signal processor (DSP). Vibrations up to 100 Hz can be generated in the platform and the base with the proof-mass actuators (PMAs) each located on the platform and the base. Two sets of tri-axial geophones, one located on the base and the other under the platform, are used to measure the vibration on the base and the platform, respectively. Both have a small inclination angle of 5° with the $+Z$-axis of the hexapod. As shown in Fig. 3, each strut consists of an active stage containing a piezoelectric actuator, a geophone sensor, and a noise filter of 1-kHz bandwidth and a passive stage consisting of layers of Beryllium-Copper for additional stiffness and viscoelastic material for damping. This passive stage provides additional isolation in case the active vibration isolation stage fails. The piezoelectric actuator used in each strut is a stack-type actuator with the operational voltage range of −15 to 150 V, operational stroke

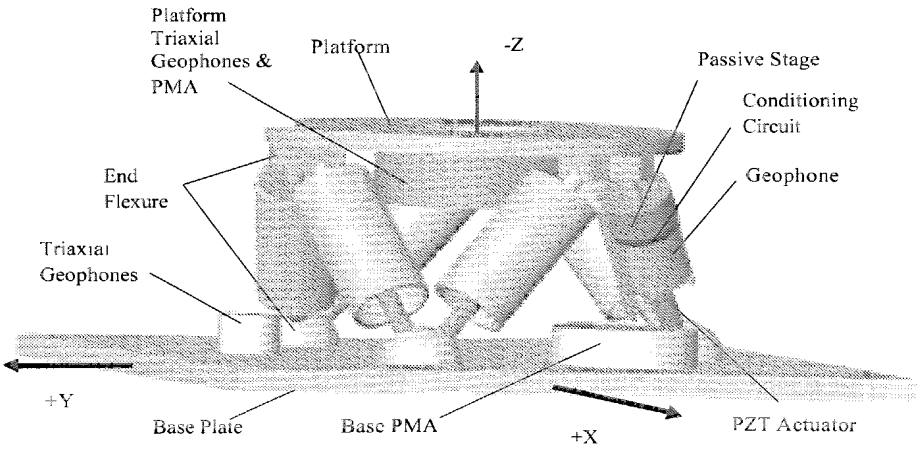

Fig. 2. The hexapod assembly consisting of a base plate, a platform, two PMAs and six struts, each with a piezoelectric actuator, a geophone sensor and a passive isolation stage.

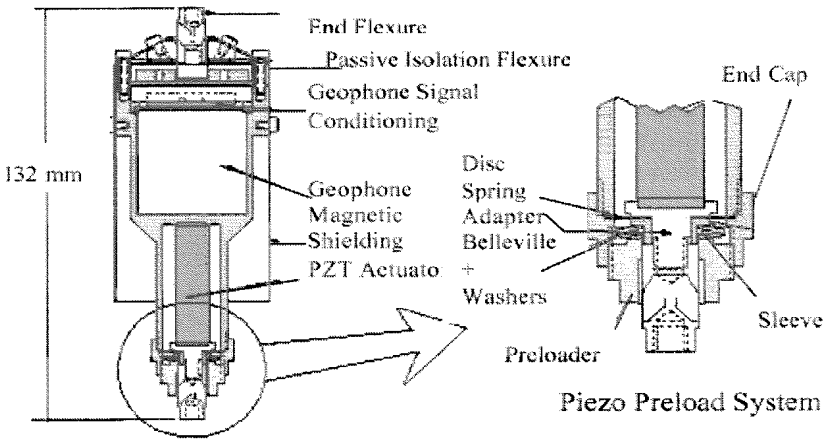

Fig. 3. A strut assembly consisting of end flexure, piezoelectric actuator, geophone sensor, signal conditioning circuit and passive isolation stage. Courtesy of United States Air Force Research Laboratory, Kirtland Air Force Base, New Mexico [1].

length of 30 μm, and resonant frequency at 1.5 kHz. The geophone sensor has the sensitivity of 0.1 V-s/mm, suspension frequency at 12 Hz above which it acts as a linear velocity sensor with 1-kHz bandwidth.

The mass of the payload suspended from the platform is 6.2 kg and the total mass of the hexapod system is 12.6 kg. An electronic data control system contains a 32-bit TMS320C31 digital signal processor manufactured by Texas Instruments. It runs on 40-MHz clock with 20-MIPS (mega instructions per second) instruction execution rate. The DSP is mainly used for the data storage, processing and calculation of control signal. The data control systems also consists of PIC16C74, an 8-bit microcontroller manufactured by Microchip that is used for the PMA actuation and temperature sensor measurement.

2.2. Software

The software for the SUITE consists of C programs, MATLAB programs, and the experiment lists. There are nine different C programs that perform the variable initialization and memory release. These subroutines are mainly used for implementing control algorithms, measuring geophone sensors and temperature sensors, and driving piezoelectric and PMAs. The experiment lists are the set of predefined commands, and are executed sequentially to perform the experiment in the particular mission. These lists provide methods of the initialization of global variables and the configuration setup before the implementation of control algorithm starts.

3. System Identification

In this section, we develop a mathematical model of the SUITE hexapod. Let $V_a = [V_{a1} V_{a2} V_{a3} V_{a4} V_{a5} V_{a6}]^T$ be the voltages applied to the six piezoelectric actuators, and $V_g = [V_{g1} V_{g2} V_{g3} V_{g4} V_{g5} V_{g6}]^T$ be the voltages read by the six geophone sensors, respectively. Hence, the relation between the voltages applied to the actuators and read by the sensors can be written in the form of a 6×6 transfer function matrix as follows:

$$\begin{bmatrix} V_{g1} \\ V_{g2} \\ V_{g3} \\ V_{g4} \\ V_{g5} \\ V_{g6} \end{bmatrix} = \begin{bmatrix} f_{11} & f_{21} & f_{31} & f_{41} & f_{51} & f_{61} \\ f_{12} & f_{22} & f_{32} & f_{42} & f_{52} & f_{62} \\ f_{13} & f_{23} & f_{33} & f_{43} & f_{53} & f_{63} \\ f_{14} & f_{24} & f_{34} & f_{44} & f_{54} & f_{64} \\ f_{15} & f_{25} & f_{35} & f_{45} & f_{55} & f_{65} \\ f_{16} & f_{26} & f_{36} & f_{46} & f_{56} & f_{66} \end{bmatrix} \begin{bmatrix} V_{a1} \\ V_{a2} \\ V_{a3} \\ V_{a4} \\ V_{a5} \\ V_{a6} \end{bmatrix}, \quad (1)$$

where f_{ij} is the transfer function from the ith input to the jth output channel. These transfer functions were found using system identification techniques that are described in the subsequent sections on the basis of experimental data obtained from all output channels. The selections of the sampling rate, the model structure and the order of the transfer function, test signals, designing and performing the experiment and mathematical model validation are the main steps to identify the transfer functions. Each step is described in the following sections.

3.1. Selection of the Sampling Rate

The Nyquist sampling theorem requires the sampling rate at least twice the closed-loop bandwidth of the

system in order to reconstruct the sampled signal faithfully. In the SUITE, the PMAs serve as sources of disturbance generation, and the overall noise level is low when all the PMAs are switched off. There is an active 2-pole antialiasing analog filter with 1-kHz bandwidth, which prevents aliasing of the high-frequency noise components in the geophone sensor measurement. The filter is located in the geophone signal conditioning circuit as shown in Fig. 3. The open-loop strut resonant frequency is 1.5 kHz. Looking at these important open-loop frequencies, the sampling rate greater than 3 kHz is desirable for the sampling of the signals. Although the sampling rate is not required to be more than the twice the open-loop bandwidth, the control becomes sensitive to the plant parameter variations and input plant disturbance at these open-loop high frequencies. The AFRL guidelines set the upper limit on the sampling rate as 5 KHz. Hence, we selected the 3.5 kHz sampling rate for all the experiments presented in this paper.

3.2. Selection of the Model Structure and the Order of the Transfer Function

3.2.1. Plant Model

The information regarding the position and the velocity of the center of the hexapod platform can be found from the lengths of the six struts and their rate of change. The six geophone sensors measure rate of change of strut lengths which can ultimately give information about the motion of the platform. Hence, it was decided to find the mathematical relation of the six piezoelectric actuator input voltages with the six strut-geophone sensor output voltages.

Initially, we tried different model structures such as ARX and ARMAX [8]. In case of an ARX model, the output at a particular time instant is dependent on the noise at the same instant. In case of an ARMAX model, the output at particular instant is dependent on the noise value at the same instant and a few past noise values. In both the cases the denominator polynomial of transfer function from the noise input to the output must be taken the same as the one for the transfer function from the control input to the output. However, the selection of the order of the transfer function relating the input to the output, and the transfer function modeling the effect of disturbance could be done independently using a BJ model. Hence, the BJ model structure was used as the identification model for every transfer function in the transfer function matrix. In order to find the order of the transfer function, the electromechanical model of the geophone sensor and the piezoelectric actuator was developed.

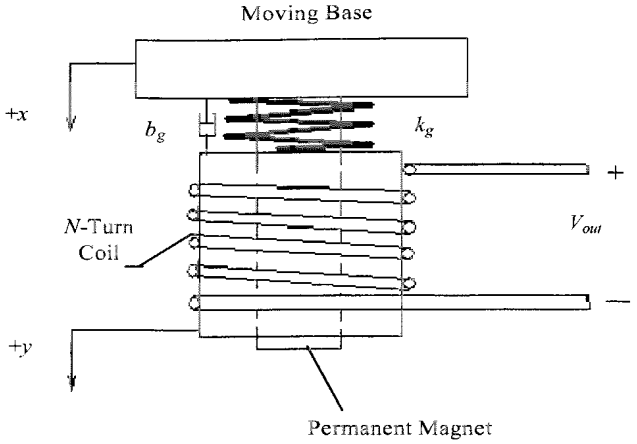

Fig. 4. Geophone sensor model. The N-turn coil suspended with the spring system moves relative to the central permanent magnet attached to the upper base.

3.2.2. Geophone Sensor Model

Figure 4 shows a model of the geophone sensor. The sensor can be modeled as the N-turn coil suspended from the base by a spring and moving with respect to the permanent magnet attached to the same base. The voltage induced in the coil is directly proportional to the velocity of the coil with respect to the magnet. Equations (2)–(4) represent the equations of the motion of the coil as a free-body, the relation between the relative velocity and the electromotive force (emf) induced in the coil, and the relation between the base motion and the induced voltage in the s-domain, respectively.

$$m_g \ddot{z} + b_g \dot{z} + k_g z = -m_g \ddot{x}, \tag{2}$$

$$V_{out} \propto n \frac{d\phi_g}{dt} = K\dot{z}, \tag{3}$$

where K is the proportional constant,

$$V_{out}(s) = \frac{-m_g K s^3}{(m_g s^2 + b_g s + k_g)} X(s). \tag{4}$$

3.2.3. Piezoelectric Actuator Model

The piezoelectric stack actuator consists of wafers of lead–zirconate–titanate (PZT) ceramic sandwiched between two electrodes. Assembling a number of such

wafers mechanically in series and connecting the corresponding electrodes electrically in parallel forms the stack. We see that there exists a rate-independent hysteresis between the voltage applied to actuator and its end-point displacement [6]. The hysteresis can be modeled by a Maxwell resistor-capacitor (MRC) circuit in the electrical domain of the electromechanical representation of the actuator because the rate-independent hysteresis is solely between the voltage applied to the actuator and the accumulated charge. Figure 5 shows the electromechanical model and Eqs (5)–(8) represent the relation between the electrical and mechanical domains of the actuator. The relation between the actuator input voltage and the displacement of the stack in the s-domain is given by (9):

$$V_{\text{in}} = V_{\text{RC}} + V_t \tag{5}$$

$$q = nx + CV_t, \tag{6}$$

$$m_{\text{p}}\ddot{x} + b_{\text{p}}\dot{x} + k_{\text{p}}x = F_{\text{t}} + F_{\text{ext}}, \tag{7}$$

$$F_{\text{t}} = nV_{\text{t}}, \tag{8}$$

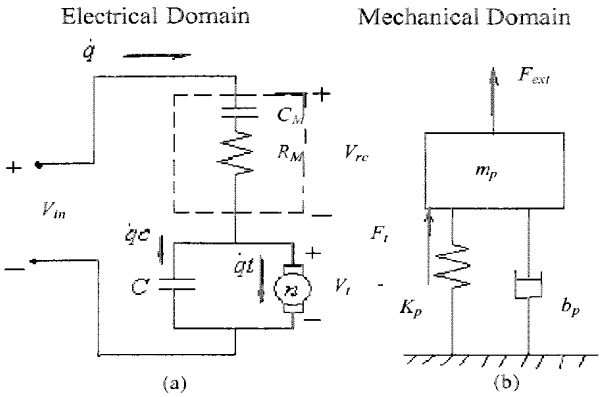

Fig. 5. (a) A model of a stack PZT actuator in the electrical domain. The circuit in the dashed box refers to the Maxwell resistor-capacitor circuit describing the hysteresis in relation to the input voltage and the charge in the circuit [6]. (b) The equivalent of the actuator spring-mass system in the mechanical domain.

$$X(s) = \left[\frac{n/C}{(m_{\text{p}}s^2 + b_{\text{p}}s + k_{\text{p}})((1/C) + (1/C_{\text{M}}) + R_{\text{M}}s) + (n^2/C)((1/C_{\text{M}}) + R_{\text{M}}s)}\right] V_{in}(s). \tag{9}$$

3.2.4. Electromechanical Model of the Combined Piezo-Geophone System

If we combine Eqs (5)–(9), the transfer function from $V_{\text{in}}(s)$ to $V_{\text{out}}(s)$ becomes

$$\frac{V_{\text{out}}(s)}{V_{\text{in}}(s)} = \left[\frac{-m_{\text{g}}Ks^3}{(m_{\text{g}}s^2 + b_{\text{g}}s + k_{\text{g}})}\right]\left[\frac{n/C}{(m_{\text{p}}s^2 + b_{\text{p}}s + k_{\text{p}})((1/C) + (1/C_{\text{M}}) + R_{\text{M}}s) + (n^2/C)((1/C_{\text{M}}) + R_{\text{M}}s)}\right] \tag{10}$$

From Eq. (10), the order of the analytical model relating the output voltage read by the geophone sensor and the input voltage applied to the piezoelectric actuator is five. Hence, the fifth-order BJ model was used to identify the collocated and non-collocated transfer functions in the 6×6 transfer-function matrix (1).

3.3. Selection of the Test Signals

A chirp signal shown in Fig. 6 with the decreasing amplitude from 25 to 5 V and the increasing frequency from 5 to 100 Hz was selected as a test signal for the identification of the transfer functions. A band-limited white Gaussian noise with its frequency contents up to 250 Hz and a pseudo-random binary signal with 150-Hz bandwidth were also used as the test signals in the process of finding the transfer functions. The maximum amplitude of each signal was limited up to ± 25 V and any voltage exceeding this range was responsible for sensor saturation. The power spectral density of chirp, white Gaussian noise, and pseudo-random sequence was above 10 dB/Hz up to 200, 400, and 175 Hz, respectively. Hence, the frequency contents of the test signals were sufficient to test broadband and narrowband vibration isolation.

3.4. Empirical Identification of the Transfer Functions

In the experiment, the test signal was applied to one actuator and all six geophone sensors were read. The

procedure is repeated by applying the test signal to each of the remaining piezoelectric actuators. The responses of all the six geophones when the chirp signal was applied to the first actuator are shown in Fig. 7. Relative magnitudes of these responses indicate that the response of a geophone sensor attached to the strut under excitation is dominant compared to the responses of other geophones. However, the response of the other geophones cannot be neglected and it shows the coupling effects among various input/output channels.

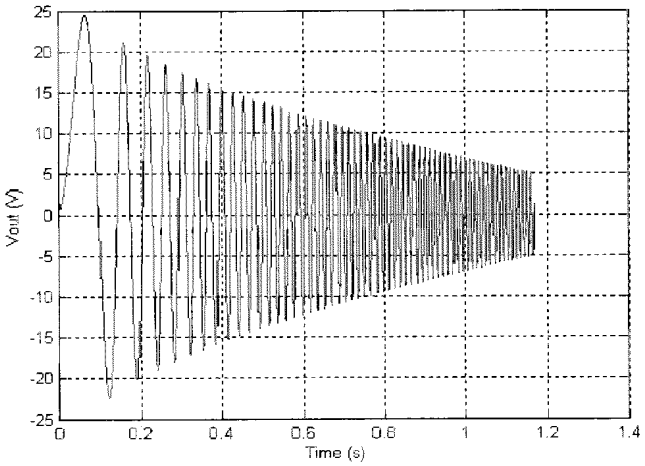

Fig. 6. The chirp signal of variable amplitude and frequency content used as one of the input signals for system identification.

We used 4096 points of the input chirp signal and the same number of the output data from geophone sensors for system identification. Using various model structures and various orders for the transfer functions ranging from 2 to 7, each transfer function represented in (1) was found. Finally we identified all the 36 transfer functions with the fifth-order BJ model structure. Equations (11)–(12) describe the transfer functions obtained when the chirp signal is applied to the second piezoelectric actuator and the output is measured from the first and the second geophone sensors, respectively.

$$f_{21} = \frac{-0.009316z(z-1.01)(z-0.9534)(z^2-2.019z+1.025)}{(z-0.06917)(z^2-1.984z+0.9879)(z^2-1.981z+0.9861)}, \tag{11}$$

$$f_{22} = \frac{2.098(z-1.006)(z-1.002)(z^2-1.96z+0.9609)}{(z+0.9914)(z-0.9597)(z-0.8325)(z^2-1.987z+0.9871)}. \tag{12}$$

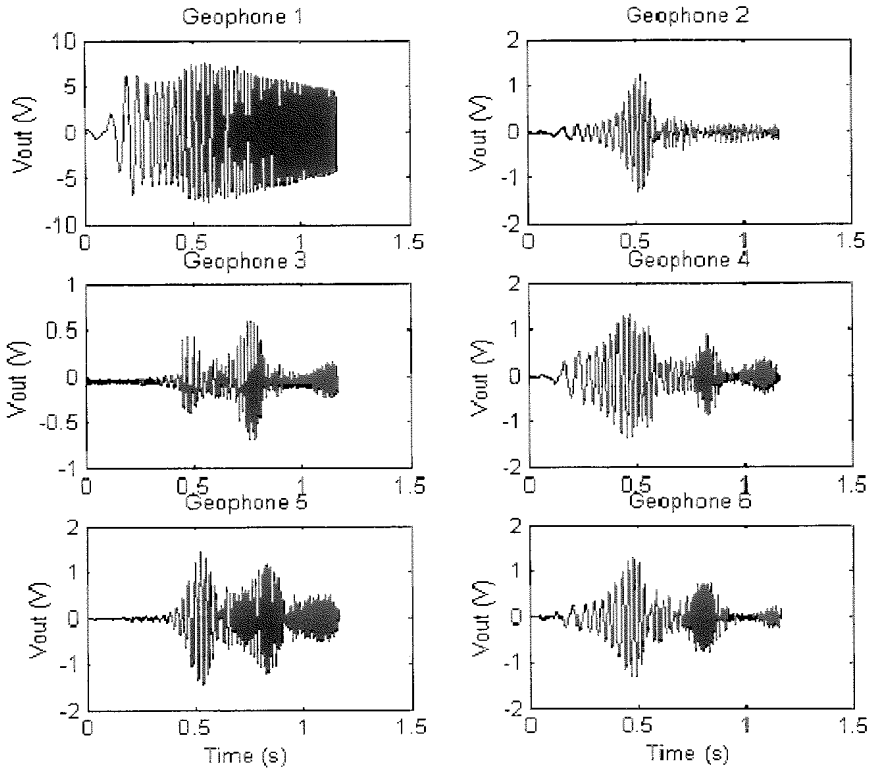

Fig. 7. Responses from all six geophone sensors when the chirp signal shown in Fig. 6 was applied to only piezoelectric actuator 1. By comparing the magnitude of the responses the level of coupling to other struts can be observed.

The obtained transfer function matrix is symmetric in nature because of the geometrical symmetry in the hexapod structure with respect to its Z-axis. Hence, f_{12} can be found, if f_{21} is known. Similarly, f_{11}, f_{33}, f_{44}, f_{55}, and f_{66} should be ideally the same as f_{22}. While performing the experiment, however these transfer functions were found individually by repeating the system identification procedure described above. Equation (12) indicates that two low-frequency non-minimum-phase zeros exist in the diagonal transfer functions of the 6×6 transfer function matrix at 3.3322 and 1.1129 Hz limiting the bandwidth of the controller. We set all non-diagonal transfer functions to zero and found non-minimum transmission zeros of multi-input multi-output (MIMO) system. They are located at natural frequencies of 1787.4698, 2.1909, 3.5742, 3.0769, 2.3597, 0.6488, 1.2365, and 3.7193 Hz. The actual response of the system was not significantly delayed nor in the direction opposite to the input. However, the presence of non-minimum-phase zeros in the model affects the performance in time and frequency-domain model validation.

3.5. Time-domain Model Validation

The simulation result obtained using the identified transfer function matrix matched very well with the actual system step response measured with the geophone sensors when step shown in Fig. 8 was applied to the system and the model. Figure 9 shows the simulated step response of the system with dotted line and experimental response with the solid line. The geophone sensor works as a velocity sensor above the suspension frequency of 12 Hz, and it shows 40 dB roll-off acting as a jerk sensor below the suspension frequency. In this case, most of the frequency contents of the step command shown in Fig. 8, are below the suspension frequency of the geophone sensor. The step response in the time interval [0.057 s, 0.114 s] is due to the rising edge of the step and the response in the time interval [0.687 s, 0.743 s] is due to the falling edge of the step. Figure 10 shows the response of the model by solid line and experimental response by dotted line when a 60-Hz sinusoid was applied to the system. The experimental response shows the cut-off in the output voltage values because our control limits

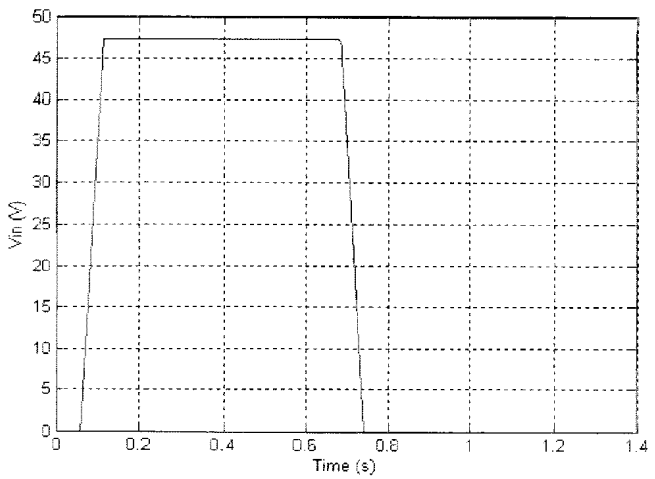

Fig. 8. Input step signal to obtain the system response in the time domain.

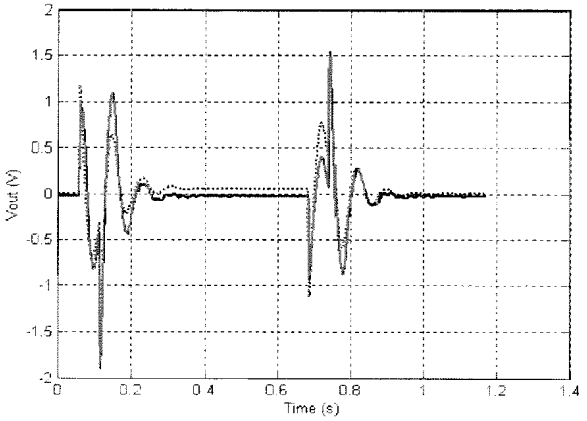

Fig. 9. Step response. The solid line indicates the step response when the experiment was run on the satellite. The dotted line is the simulated output when the step input was applied to the transfer function model obtained using the chirp signal shown in Fig. 6.

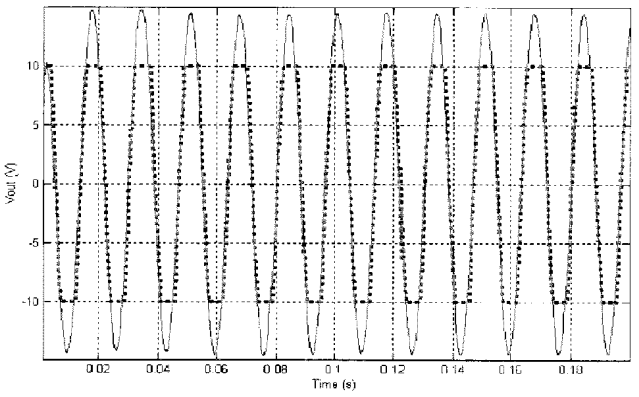

Fig. 10. The response of system to a 60-Hz sinusoidal input. The dotted line represents the response of the actual experiment and the solid line is the simulated output by the transfer function obtained using the chirp signal shown in Fig. 6. The dotted line is truncated beyond ± 10 V to avoid sensor and actuator saturation.

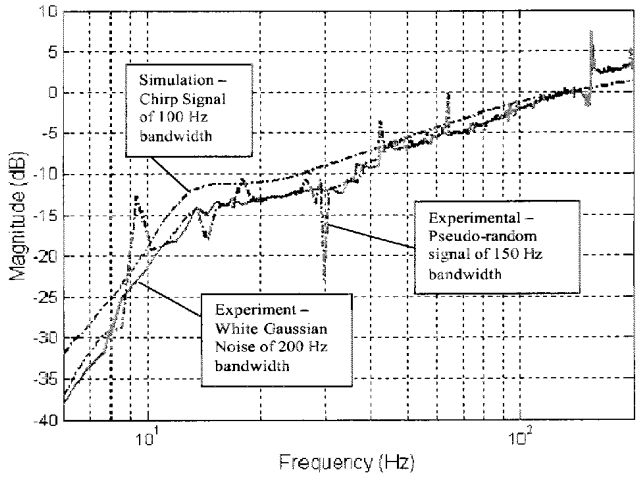

Fig. 11. Frequency-domain validation. The solid line indicates the Bode plot for identification of the transfer function using band-limited white Gaussian noise, the dash-dotted line indicates the Bode plot of the identified transfer function when a band-limited pseudo-random binary signal is used, and the dotted line indicates the Bode plot of the transfer function obtained using a fifth-order BJ model with a chirp signal.

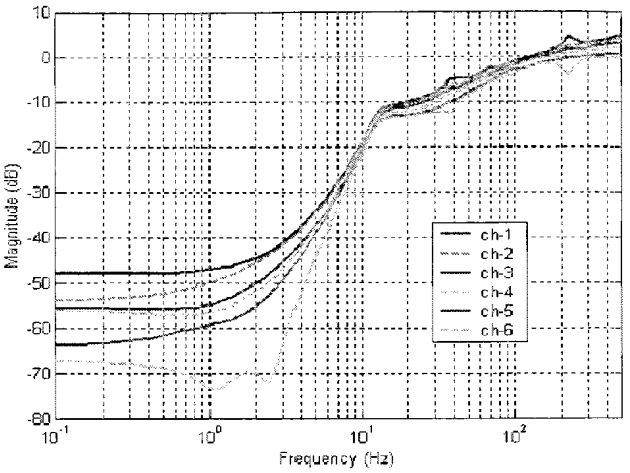

Fig. 12. Singular-value plot for the nominal plant transfer function matrix G showing a band of singular values up to 500 Hz.

the voltage output to ± 10 V to avoid the sensor and actuator saturation.

3.6. Frequency-domain Model Validation

In order to validate the transfer functions obtained in (11)–(12), frequency-domain model validation was also carried out. A band-limited white Gaussian noise with 250-Hz bandwidth and a pseudo-random binary signal with 150-Hz bandwidth were also applied to the system and the outputs were observed. Figure 11 shows the Bode magnitude plots of the transfer function given by (12) obtained using a chirp signal, and the estimates of the transfer function obtained using a band-limited white Gaussian noise and the pseudo-random binary signal. They match well in the frequency range of [10 Hz, 250 Hz].

4. Controller Design Methodologies

4.1. Analysis of Identified Transfer Function Matrix

The singular value analysis of a 6×6 transfer function matrix of the hexapod system is shown in Fig. 12. The maximum and the minimum singular value plot form a band of the singular values of the system at a particular frequency. In the frequency range of [0.1 Hz, 5 Hz], the singular-value band is broad

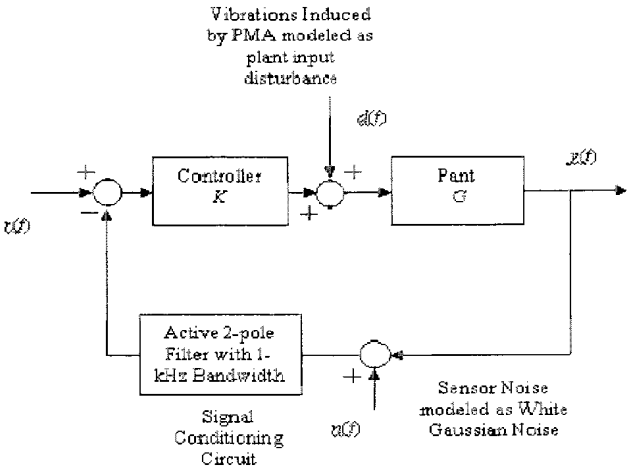

Fig. 13. Continuous-time feedback control system with $r(t)$ as the reference input, $y(t)$ as the output, $d(t)$ as the plant disturbance, and $n(t)$ as the measurement noise.

denoting the maximum directional dependencies in the system. In the frequency range of [5 Hz, 25 Hz], this band is narrow denoting the minimum directional dependency. The nominal plant performance justifies the requirement of the augmentation of the plant dynamics with the controller dynamics for achieving the desired performance specification. In the strut assembly, the piezoelectric actuator and the geophone sensor form the plant G. Figure 13 presents a closed-loop model of the system, where K is the controller to be implemented. The controller

works on noisy sensor measurements with zero-reference input. The output of the geophone sensor is noisy and the noise $n(t)$ is modeled to enter at the output. There is no reference to be tracked and hence $r(t)$ will be zero in the ideal case. The vibrations are induced using the PMA on the base and these vibrations can be modeled as disturbance $d(t)$, injected at the entry of the plant. Equations (13)–(14) describe the relation among the output $y(t)$, and the sensor noise $n(t)$, the reference to be tracked $r(t)$ and the input disturbance $d(t)$.

$$y(s) = (I + GK)^{-1}GKr(s) + (I + GK)^{-1}Gd(s) - (I + GK)^{-1}GKn(s), \tag{13}$$

$$y(s) = Tr(s) + SGd(s) - Tn(s), \tag{14}$$

where

$L = GK$ defined as the loop shaping transfer function,

$T = \dfrac{GK}{1+GK} = \dfrac{L}{1+L}$ defined as complementary transfer function and,

$S = \dfrac{1}{1+GK} = \dfrac{1}{1+L}$ defined as sensitivity transfer function.

Hence, the problem of active vibration isolation reduces to shaping the singular value band of the sensitivity transfer function as low as possible up to 100 Hz.

4.2. MIMO Controller Design Methods

Using multivariable controller design techniques such as LQG/LTR and H^∞ control [2,12,14], controllers were designed and their performances were verified. The design of LQG/LTR compensator was based on optimal control gain and Kalman filter gain where input plant disturbance matrix and covariance matrix for sensor noise were selected as design parameters. The covariance matrix representing the sensor noise is assumed to be an identity matrix with a multiplicative factor of 0.01. The multiplicative factor was calculated by repeatedly reading all geophone sensors without applying any external input and taking the mean of their standard deviation values. By solving a Kalman-filter and optimal-control dual problem, the LQG/LTR controller was designed. When a 5-Hz sinusoid of unit amplitude was applied to the six channels simultaneously for two seconds in the simulation of LQG controller, the vibration was attenuated effectively by 33 dB. Figure 14 shows the vibration attenuation at all six channels and the settling of the system after two seconds. The simulation results of LQG controller was satisfactory at 5 Hz, however, the vibration attenuation at 25 and 100 Hz frequency were not satisfactory. The controller designed using LQG/LTR had limited loop transfer function recovery due to the presence of the non-minimum-phase zeros in the plant.

In order to achieve the robustness in the controller design, the H^∞ controller was designed. The objective of the design is to minimize the infinite norm of the matrix N given by (15):

$$N = \begin{bmatrix} W_2KS \\ T \\ W_1S \end{bmatrix}, \tag{15}$$

where W_1 and W_2 are design parameters and their value is selected as follows:

$$W_1 = 0.0001\frac{(s+10)}{(s+1)(s+100)}I^{6\times 6}, \tag{16}$$

$$W_2 = 0.00001I^{6\times 6}. \tag{17}$$

The matrix N is the cost function and the matrices W_1 and W_2 are the weights for the error signal and the control signal in the cost estimation function. In this particular case, W_2 is assigned a constant value over all frequency range and W_1 is assigned a higher weight in the lower frequency range. The lower magnitude of W_2 matrix denotes that there is less weight for control input in the minimization of the infinite norm of the matrix KS. The particular value (1×10^{-5}) for the coefficient of W_2 matrix is selected in order to relieve the specification constraints on KS. However, the Bode plot of each diagonal transfer function of W_1 shows that the higher weight is given to error signal up to 25 Hz. The constraints on the sensitivity S are relieved for frequencies above 25 Hz. In the simulation, H^∞ controller achieved 33- and 13-dB vibration attenuation at 5 and 25 Hz respectively. Figure 15 shows the vibration attenuation observed at all six channels and settling of the system after two seconds when a 25-Hz sinusoid was applied to all channels.

The main challenge was to implement the MIMO control algorithms efficiently without occurrence of the frame overrun. The sampling rate of 3.5 kHz was used throughout the experiment. It was equivalent to 285 μs of the intersampling time. The SUITE hardware and software was designed such that the half of the intersampling time was used for the background

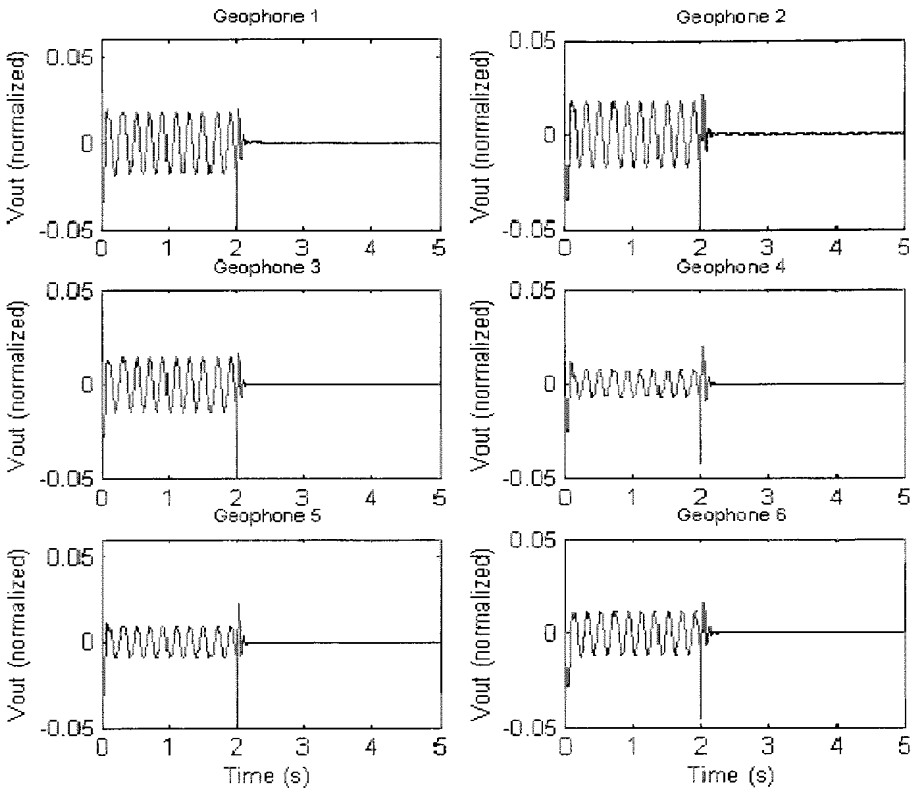

Fig. 14. The responses of six output channels with the LQG/LTR controller when a 5-Hz sinusoid was applied as the input plant disturbance.

work such as memory release, global variable access, and data population, and the rest half was used for the actual control algorithm implementations. It implies that the 142-μs time is available for the controller implementation. The TMS320C31-40 DSP has 20-MIPS execution rate, which implies that the 50 ns is required for the execution of every instruction. In 140 μs, maximum 2800 calculations can be performed. The high-order MIMO controllers could not be implemented because of the limitation on current computation power. Also, performance of SISO controllers such as lead-lag compensator and notch filter was not satisfactory at 100 Hz due to the presence of non-minimum phase zeros on every diagonal transfer function of 6×6 transfer function matrix.

5. Conclusions

The 6×6 transfer function matrix for a six-input six-output was identified in the discrete-time domain with the help of bandlimited chirp signal, white Gaussian noise, and pseudo-random binary sequence. ARX, ARMAX, and BJ model structures were used to identify the transfer function matrix. The fifth-order BJ model structure obtained all the transfer functions whose simulated responses matched well in the time-domain. Also, the Bode plot of transfer functions identified by the chirp signal matched well with the bode plots obtained from pseudo-random binary sequence and white Gaussian noise in the 5–200 Hz frequency range. The frequency-domain validation was done only in the limited frequency range because the bandwidth of all the test signal was limited up to 250 Hz. The fifth-order of the transfer function was the same as the order of transfer function of the piezo-geophone electromechanical model.

The multivariable controllers were developed using LQG/LTR and H^{∞} controller design techniques. Because of the limitation of computing and processing power of the present hardware, these high-order multivariable controllers could not be implemented on the satellite. However, the simulated responses of these implementations show 33, and 12 dB attenuation at 5 and 25 Hz, respectively, and supported the validity of identified transfer function matrix.

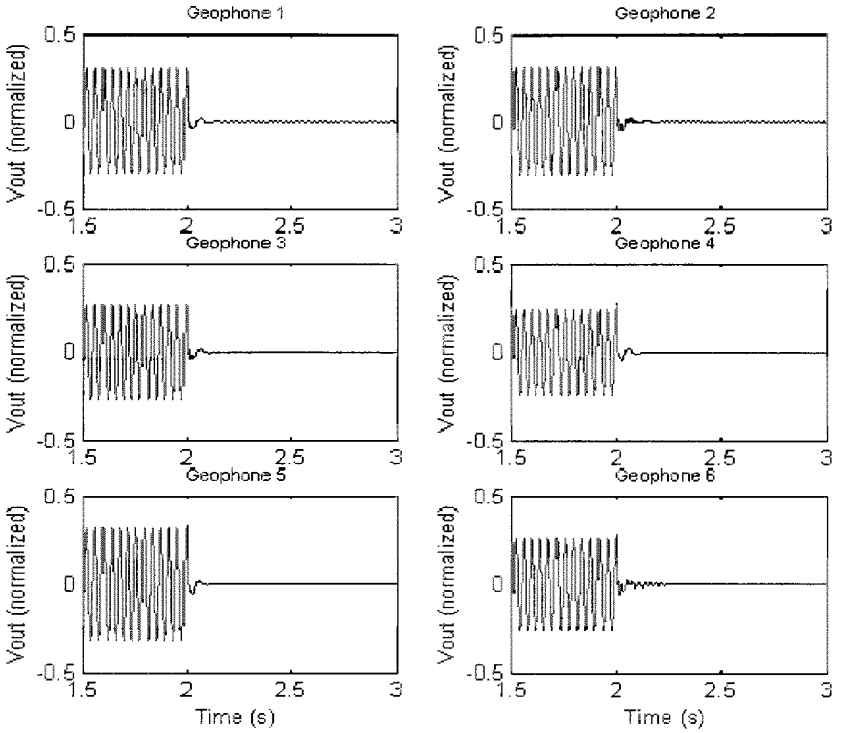

Fig. 15. The responses of six output channels with the H^{∞} controller when a 25-Hz sinusoid was applied as the input plant disturbance.

Acknowledgments

We thank Dr. R. Scott Erwin at Air Force Research Laboratory/VSSV for his technical support through the SUITE Guest Investigator Program. We would also like to thank Ms. Leslie Sullivan who helped us conduct the experiments on the ground unit and on the satellite, and promptly solved various technical and non-technical problems while performing the experiments.

References

1. Air Force Research Laboratory, Space Vehicle Directorate. Satellite ultraquiet isolation technology experiment (SUITE). Guest Investigator's Handbook, 1999, pp 1–16
2. Athans M. A tutorial on the LQG/LTR method. Proceedings of american control conference, 1986, pp 1–8
3. Erwin SR, Anderson EH, Fumo JP. Satellite ultraquiet isolation experiment. Proceedings of IEEE, 2000, pp 299–312
4. Fuentes JR, Shrader KN, Balas MJ, Erwin SR. Direct adaptive disturbance rejection and control for deployable space telescope, theory and application. Proceedings of American control conference, 2001, pp 3980–3985
5. Geng JZ, Haynes LS. Six degree-of-freedom active vibration control using the stewart platform. IEEE Trans Control Syst Technol 1994; 2(1): 45–53
6. Goldfarb M, Celanovic N. Behavioral implications of piezoelectric stack actuators for control of micromanipulation. Proceedings of IEEE, 1996, pp 226–231
7. Lauffer JP, Hinnerichs TD, Kuo CP, Wada B, Ewaldz D, Winfough B, Shankar N. Milling machine for the 21st century – goals, approach, characterization and modeling. Proc SPIE 1996; 2721: 326–340
8. Ljung L. System identification, theory for user, 2nd edn. Prentice Hall, New Jersey, 1999
9. Nanua P, Waldron KJ, Murthy V. Direct kinematical solution of stewart platform. IEEE Trans Robotics Autom 1990; 6(4): 483–444
10. Nguyaen CC, Zhou Z, Antrazi SS, Cambell CE. Efficient computation of forward kinematics and jacobian matrix of stewart platform-based manipulator. Proc IEEE, Southeastcon 1991; 2: 869–874
11. Pernechele C, Bortoletto F, Reif K. Hexapod control for an active secondary mirror: general concept and test results. Appl Opt 1998; 37(28): 6816–6821
12. Safonov M. Stability and robustness of multivariable feedback system. 2nd edn. The MIT Press, Cambridge, 1980
13. Saranli U, Buehler M, Koditschek DE. Design, modeling and preliminary control of compliant hexapod

robot. Proc IEEE Int Conf Robot Autom 1999; 3: 2589–2596
14. Skogestad S, Postlethwaite I. Multivariable feedback control, analysis and design. John Wiley and Sons, 1997
15. Svinin MM, Hoseoe S, Uchiyama M. On the stiffness and stability of gough-stewart platforms. Proc IEEE Int Conf Robot Autom 2001; 4: 3268–3273
16. Trucco R, Pepe F, Galeone PC. Hexapod pointing system. Proceedings of the 3rd International Conference on Spacecraft Guidance, Navigation and Control systems 1996, pp 201–208
17. Warnecke HJ, Neugebauer R, Wieland F. Development of hexapod based machine tool. CIRP Ann, Manufacturing Technol 1998; 47(1): 337–340
18. Watson LT. Globally convergent homotopy algorithms for nonlinear systems of equations. *TR 90-26*, Department of Computer Science, Virginia Polytechnic Institute and State University, Blacksburg, VA, 1988
19. Williams RL. Kinematics of an in-parallel actuator manipulator based on stewart platform mechanism. NASA Technical Memorandum 107585, Hampton, VA 1992, pp 1–28